RF Rectifier Toward Terahertz Integrated Image Detector

Volha Varlamava[1], Giovanni De Amicis[2], Andrea Del Monte[2], Rosario Rao[1(✉)], and Fabrizio Palma[1]

[1] Department of Information Engineering, Electronics, Telecommunications, Sapienza University of Rome, Eudossiana str. 18, 00184 Rome, Italy
varlamava@die.uniroma1.it, rosario.rao@uniroma1.it, palma@diet.uniroma1.it

[2] LFoundry S.r.l, A. Pacinotti str. 7, 67051 Avezzano, Italy
{giovanni.deamicis,andrea.delmonte}@lfoundry.com

Abstract. We present a new CMOS compatible direct conversion terahertz detector operating at room temperature. The rectenna consists of an integrated antenna, realized on the surface of the integrated circuit and connected to a nanometric metallic whisker at one of its edges. The whisker reaches the semiconductor substrate that constitutes the antenna ground plane. The rectifying device can be obtained introducing some simple modifications of the charge storage well in conventional CMOS APS devices, making the proposed solution easy to integrate with existing imaging systems. No need of scaling toward very scaled and costly technological node is required, since the CMOS only provides the necessary integrated readout electronics. On-wafer measurements of RF characteristics of the designed rectifying junction are reported and discussed.

Keywords: Image detector · THz antennas · Rectifying antenna (rectenna) · Double barrier junction

1 Introduction

THz imaging and spectroscopy applications have a great potential in time-domain spectroscopy [1], communications [2], security control [3], and biomedical imaging [4]. For this reason in past decades a great interest of the research community has been attracted by this region of the electromagnetic spectrum, pushing the microwave and optical THz devices through a constant progress in the development and the improvement of detectors in terms of noise equivalent power.

Currently the main interest is the development of low cost, fast, highly sensitive, compact and room temperature THz detectors. The feasibility of rectifying antennas (rectennas) for the detection of freely propagating THz radiation has been demonstrated [5]. The radiative part of these devices is typically formed by an antenna that focuses the energy of the impinging electromagnetic field into a localized spot called active region, where the rectifying element is placed. The latter produces a continuous current proportional to the energy of the impinging electromagnetic wave.

© Springer International Publishing AG 2018
B. Andò et al. (eds.), *Sensors*, Lecture Notes in Electrical Engineering 431,
DOI 10.1007/978-3-319-55077-0_7

Recently we presented a new structure resulting from the integration of a 3D antenna with widely produced commercial CMOS image detector [6]. The fabrication process, described in [7], permits to integrate the three dimensional antenna directly on the surface of the chip, by means of MEMS technology, and ensures a very low parasitic capacitance, because of the distance between antenna spires and the chip surface.

A further step of the development of this THz technology is the development of low cost, fast, highly sensitive, compact and room temperature detectors. The integration in arrays, in standard CMOS technology, is also mandatory to make exploitable readout and elaboration electronics capabilities. This paper presents a new approach resulting from the direct integration of the antenna with a rectifying device obtained by modification of commercial CMOS Image Sensors (CMOS ISs) [8].

Nowadays CMOS Image Sensors (CMOS ISs) are predominant electronic devices in the field of digital imaging [9]. The photosensitive element of the pixel is the pinned photodiode, i.e. a p-n-p structure constituting the charge storage well (SW) dedicated to the photocurrent integration during the exposure time. In the readout cycle the integrated charge is transferred to a capacitance ("floating diffusion", FD) inducing a voltage difference that is sampled with a transistor in source follower configuration. The complete charge transfer from photodiode to the floating diffusion allows the elimination of the thermal reset noise of the capacitor, referred as kTC noise, by means of the correlated double sampling. This property in combination with the extremely low dark current produced by pinned photodiode contributes to the high image quality of CMOS ISs.

The semiconductor structure implemented in the detector is suitable to perform the rectification of terahertz radiation and to permit accumulation of the rectified charge into a storage capacitance and its readout, by means of a technology compatible with CMOS ISs. The rectifying device with vertical extension of few tenths of nanometers can be created at the base of the nano-whisker previously described, using one of its metal edges as part of the electronic device itself.

This work is organized as follows. In Sect. 2, the structure of the detector is presented and its principle of operation is discussed. Section 3 is dedicated to the presentation of a test structure of the rectifying device and to the characterization of its performance. The effect of doping distribution due to different implantation processes is presented.

2 The Rectifying Device

In Fig. 1 the structure of the rectenna and its connection with the photodetector is presented. The structure is designed as a combination of an antenna fabricated on the surface of the chip with a rectifying junction capable to produce the direct conversion of terahertz electromagnetic field into dc current [10]. The necessity to adopt an approach as close as possible to the existing CMOS photodetectors technology suggests to use a rectifying semiconductor structure realized by a double barrier formed by the metal of the whisker, chosen with working function similar to an n^+-doped semiconductor, a properly designed p^+-doped surface layer and by the weakly n-doped

semiconductor of the storage well (SW). Both the SW and the p^+-type implanted surface layer are commonly used in CMOS image detectors respectively to collect the detected charge and to separate it from the semiconductor surface [9].

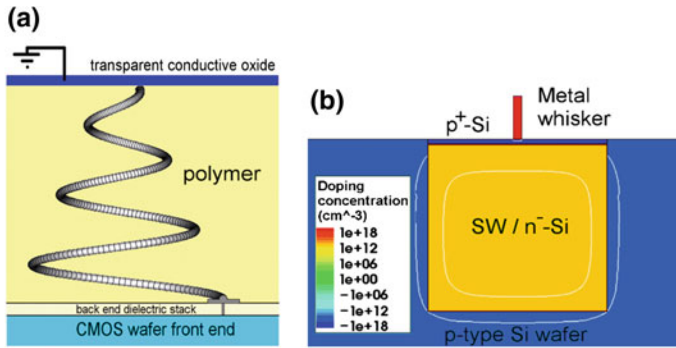

Fig. 1. **a** Schematics of rectenna geometry; **b** front view of the metallic whisker facing the storage well

In the double barrier, a rectifying effect arises from the different extension of two depletion regions, very short for the so called “first junction”, formed between the metal and the p+ layer, and much more extended for the so called “second junction”, formed between the p^+-doped layer and the SW. The rectifying effect can be explained as follows: the electric field variations induced by the antenna and focused by the whisker on the rectifying device, induce variations of voltage drop through the depleted zones of the two barriers. The majority of the voltage drop occurs through the second depletion region, mainly extending into n-doped region of the SW, much wider that the depletion region related to the first junction. As a consequence, with positive voltage applied to the metal, a reduction of the barrier of the second junction occurs, and electrons preliminarily stored in the SW can be extracted. On the contrary, with negative voltage, electrons present in the metal layer are injected in a much lower number into SW, since the barrier of the first junction is reduced by a much smaller amount due to its shorter extension.

Numerical simulations of the semiconductor device were performed by means of Synopsys Sentaurus TCAD tools using the two-dimensional hydrodynamic model. This model includes “hot electron” phenomenon that become important in submicron devices. It is not included in the conventional drift-diffusion model. Moreover, the hydrodynamic model reproduces the velocity overshoot effects. Simulator engine allows to perform 2.5D simulations setting to 100 nm $\times$ 100 nm the area of the metal contact. As reference, these contact dimensions are achievable by means of 193 nm ArF DUV photolithography process. The use of a not deeply scaled CMOS technology is not a limiting factor. In fact, simulations results [11] demonstrate that these dimensions are suitable to achieve a very high focusing capability of the antenna coupled to the device, and that a further reduction would not bring to a substantial advantage.

Since the structure is supposed to be zero-biased, the resulting barrier must be sufficiently low in order to produce an appreciable rectified current, even under presumably low voltage variations induced by the THz radiation. Figure 2 reports the 2D distribution of conduction band energy besides the rectifying device, assuming a p^+-doped region 30 nm thick, with constant doping concentration of 1.0E18 cm^{-3}. The presence of the barrier along the vertical central cut of the contact is easily observed.

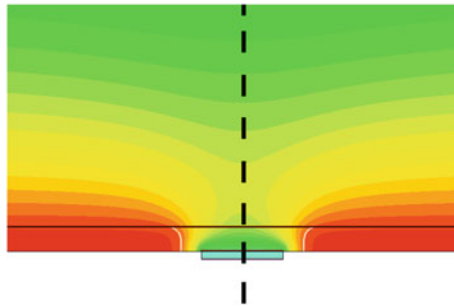

Fig. 2. 2D plot of conduction band energy inside the region in which the rectification takes place. Distribution calculated in equilibrium state with titanium metallic contact

Figure 3 reports the amplitudes of electrons current densities induces by 50 mV voltage variations applied to the metallic contact, with the p-type substrate connected to ground, as simulated by TCAD, along the 1D cut shown by the dashed line in Fig. 2. Curves are obtained for different frequencies between 1 GHz and 1 THz.

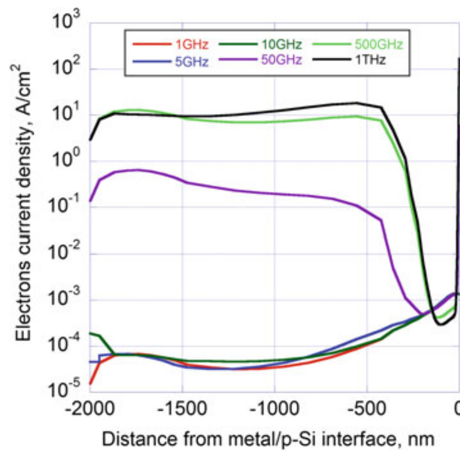

Fig. 3. Amplitude of electrons current densities variations along a section of the rectifying barrier

For all curves, one can note a relevant frequency dependence of the electrons current density at the contact (i.e. calculated at distance zero from the metal/p-Si interface) and inside the SW. In particular, electrons current density at the contact is higher at higher frequencies, as expected due to the presence of the barrier capacitance in series to the contact. At each simulated frequency, the electrons current density is lower inside the SW that at the contact, that is the effect of the current redistributing over a larger section. A saturation effect is evident over 500 GHz; it can be attributed to the resistance of the SW that limits the current at higher frequencies. Furthermore, over 500 GHz we observe the thinning of the depletion layer at the junction, caused by the lack of the charge fed to the barrier depletion layer. With the decrease of the frequency the electrons current inside the SW drops dramatically, due to the effect of the distributed capacitance that SW forms with the surrounding substrate.

It is important to notice that the electrons current across the barrier remains unchanged up to around 500 GHz, and with greater evidence at 1 THz, where the current start decreasing. In these cases, semi-periods of the excitation signal equal to, respectively, 1 and 0.5 ps, become shorter than the time of flight of electrons through the barrier [12].

The rectification capability of the structure is demonstrated in Fig. 4, where a magnification of simulated curves of electrons current density absolute values beside the junction barrier is presented. Reported values are evaluated at the end of two linear voltage ramps, the positive one going between 0 V and 50 mV (continuous line) and the negative one going between 0 and −50 mV (dashed line). Different colors represent voltage ramp rise time of 1 ns, 100, 10 and 1 ps. All curves in Fig. 4 are simulated with SW contacted to ground by means of an ohmic contact, so that there is no current drop effect at low frequencies due to SW capacitance.

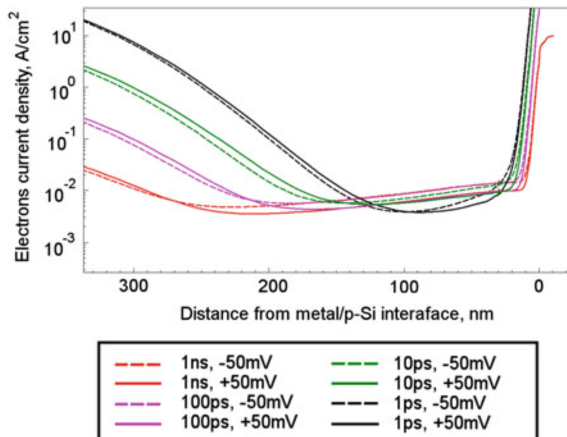

Fig. 4. Absolute values of the electrons current density along the section of the rectifying barrier induced by voltage ramps with different characteristics

One can note that the residual electrons current density through the barrier is many orders of magnitude below the absolute current density injected at the contact; nevertheless, the difference between values of this conduction current density calculated under positive and negative solicitation ramps is of up to about 50%. The rectification effect of the device is supposed to be due to this difference.

In Fig. 4, an increase the rectified current can be observed as the voltage ramp rise time changes from 1 ns to 10 ps. This increment represents an effective improvement of the rectifying capability, which can be explained as due to the decrease of the depletion layer at higher values of voltage ramp rates, i.e. at higher frequencies.

Curves derived for 1 ps rise time show the decrease of electrons current density beside the rectification region. This phenomenon can be explained observing that 1 ps rise time is shorter than the time of flight of electrons through the barrier. The resulting drop of the number of electrons crossing the barrier within the ramp time produces the drop of the current.

3 On-Wafer Measurements

We developed a test structure to verify the rectification properties of the detector. The test structure, reported in Fig. 5, does not include the antenna and is designed for tests at frequencies well below THz range in order to be handled with standard microwave probes and available instrumentation. The signal is applied by a radio frequency generator to emulate the excitation coming from the receiving antenna. This latter measurement setup choice may appear somewhat arbitrary, however in the following we show that with proper modelling it is still possible to provide expected results at THz range combining RF range measurements and numerical simulations.

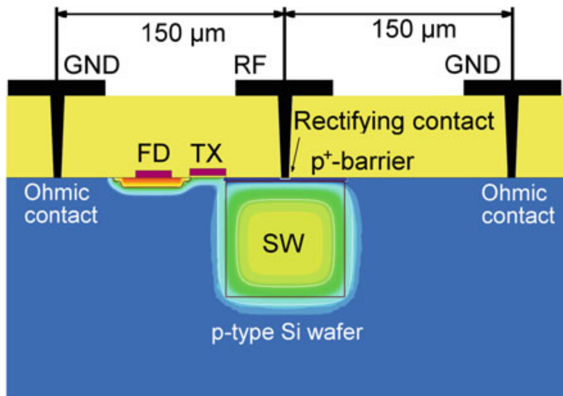

Fig. 5. A schematic description of the test structure. Dimensions of the RF and GND pads and of SW are not in scale

The test structure is realized with minor changes from a standard configuration of a CMOS commercial photodetector using the Aptina/ON Semiconductor 0.15 μm

technology node. The additional technological step requested for the pixel reconfiguration for THz range operation consists in an extra p-type doping implantation below the whisker, forming the p^+-Si layer described in the previous section. The main effect of this step is the barrier height and shape trimming, the phenomenon that hardly affects the rectifying capability of the device. Such implantation can be performed through a properly designed window through which also the metal used for the realization of contact, titanium (Ti), is further deposited. Metal deposition is performed to obtain a via hole between the pad metallization and the rectifying contact. Figure 6 reports layout and SEM cross-section image of the detector, with the SW, metal whisker, rectifier and the TX transistor. Labels TX and FD denote, respectively, the gate and the floating diffusion nodes of transfer gate transistor included in the standard photo detector configuration.

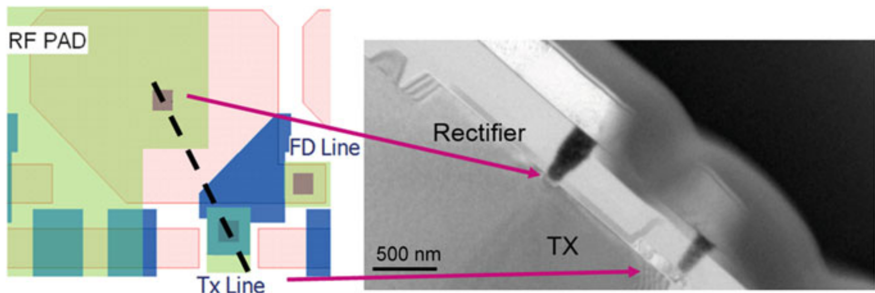

Fig. 6. Layout and SEM cross-section of SW, metal whisker rectifier and TX transistor

Finally, at top metallization level, a planar pattern with three pads is realized with sizing suitable to be contacted by standard RF microprobes. In particular, Microtech Cascade ACP-150 GSG microprobes were used during measurements. The central pad (labeled RF in Fig. 5) is connected to the rectifying contact to be tested, and the two external pads (labeled GND in Fig. 5) are electrically connected to the p^+-Si layer and to the doped substrate surrounding the SW, by means of via holes and ohmic contacts.

The equivalent circuit of the measurement setup is shown in Fig. 7. The gate voltage on TX gate node, V_{TX}, switches the transistor between two states: in TX OFF state the SW is isolated from FD node, permitting the accumulation of the rectified charge, meanwhile in TX ON state the transfer of the accumulated charge from SW to the readout node is performed. Capacitances of FD and of SW are denoted as C_{FD} and C_{SW}, respectively. A Keithley 617 pico-ammeter, shown by the circled capital A, is connected to FD through a low pass filter, represented by the inductance L_{LPF} connected in series.

In order to test experimentally the device rectification capability and to evaluate the rectification efficiency, we performed measurement on two samples with different parameters of the p-type doping implantation, as reported in Table 1. In particular, sample 4E had a higher dose and lower energy with respect to sample 1C. All measurements reported in the following are performed at test frequency of 40 GHz.

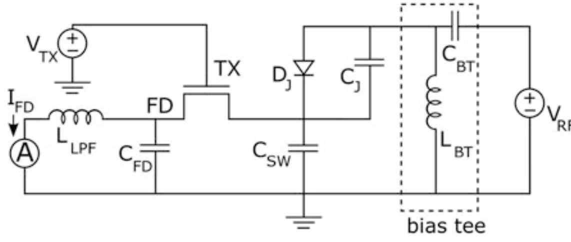

Fig. 7. Equivalent circuit of the measurement setup

Table 1. Implantation scheme

Group	Energy, keV	Dose, cm^{-2}
1C	13.5	1.0E13
4E	5.0	5.0E13

Figure 8 reports the rectified current measured by pico-ammeter versus the RF power applied to the signal pad, for 4E and 1C devices. The voltage level at TX gate node was 4 V for both curves, ensuring TX ON state.

A linear approximation of curves in Fig. 8 can be used to evaluate the detector efficiency. We approximate as linear the relationship between the RF power expressed in decibel-milliwatts, P_{dBm}, and ten times the logarithm of the current, I_{dBA}, as given by

$$P_{dBm} = P_{dBm,0} + k\left(I_{dBA} - I_{dBA,0}\right), \quad (1)$$

where ($P_{dBm,0}$, $I_{dBA,0}$) is an arbitrary chosen reference point on (P_{dBm}, I_{dBA}) curve, and the coefficient k can be calculated from geometrical regression of measured data. Figure 8 shows a different slope of the two curves.

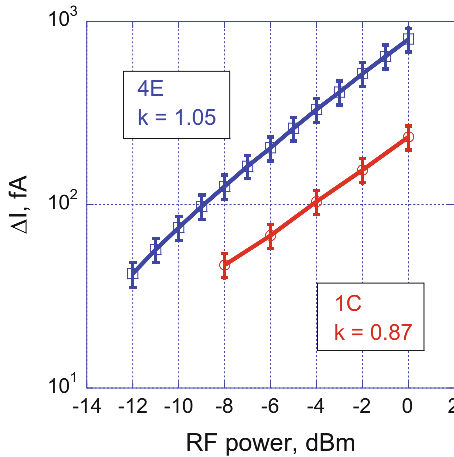

Fig. 8. Rectified current versus applied RF power for the two structures: 4E and 1C

Recalling that the plot is logarithmic, the different k means a different exponential coefficient in the nonlinear relationship rectified current —RF power. This parameter allows to account the actual modulation of the barrier under the rectification process. From the sample 4E we obtained $k = 1.05$, while for the sample 1C the coefficient resulted $k = 0.87$. This effect can be explained as due to the steeper and superficial distribution of the superficial dopant in sample 4E if compared to the sample 1C. As highlighted by TCAD process simulations, the higher dose and the lower energy of the implantation process lead to the rectifying device with higher but more asymmetric double barrier. As the rectification efficiency is strongly affected by the asymmetry degree of the barrier, the obtained rectified current is higher for the sample 4E, although its greater barrier height. At large RF power values, the deformation of the barrier partially compensates the higher current expected in the lower barrier of the sample 1C. Nevertheless, the values of sensitivity calculated for the two samples are comparable due to different k values.

Numerical simulations the semiconductor device reported in Fig. 3 can be used jointly with measurements in Fig. 8 to evaluate the noise equivalent power (NEP) of the sensor.

From the measurements, we may extract the 40 GHz voltage applied to the junction by the RF power generator. For the sake the test structure S_{11} measurement, obtained with an input power of −10 dBm and reported in Fig. 9, is used.

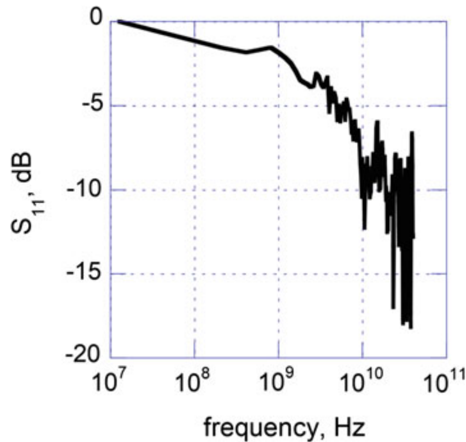

Fig. 9. Scattering parameter S11 measured on the RF test pad

The measure indicates the good matching of the structure at frequencies between 10 and 40 GHz, meaning that the real part of the test structure is nearly 50 Ω, mostly due to the series resistance of the semiconductor structure. S_{11} has a cutoff frequency of $f_H = 1$ GHz, thus at 40 GHz most of the voltage drops onto the resistance. The voltage applied to the pad and to the rectifying structure can be approximated by:

$$V_J \cong \sqrt{\frac{2R_S}{P}\frac{f_H}{f}}, \qquad (2)$$

where V_J is the voltage at the rectifying junction, P is the applied RF power, R_S is the series resistance of the test structure. This expression takes into account its one-pole behaviour with respect to the voltage imposed by the RF voltage generator.

From measurements reported in Fig. 8 we extrapolate that the RF power at 40 GHz necessary to generate a rectified current equal to the noise current. The latter, defined as a mean square value of noise measure in photodetector, was measured to be of 5 el/s, value comparable with data reported in literature [9]. For sample 4E, we find a noise equivalent RF power of −60 dBm. Accordingly to (2), this power corresponds to a voltage drop at the rectifying junction of 7.9 μV.

The rectified current depends dramatically on the shape and the height of the barrier. The nonlinearity parameters were thus obtained directly from the measurements. Besides that, from the simulation we extract the frequency behavior in order to extend the results at 1 THz. We note that simulations reported in Fig. 4 clearly indicate that, under the same amplitude of voltage applied to the junction, the rectified current has the same value for a ramp of 25 ps (as interpolation from the 10 and 100 ps curves) and for the ramp of 1 ps. Thus we can extend at 500 GHz, the value of 7.9 μV as the voltage at the junction necessary to equate the noise. We can now use the simulation of Fig. 3 to scale down the value of the density of current at the contact at this frequency. From the amplitude of 167 A/cm^2, obtained under 50 mV solicitation, scaled to the voltage value just found of 7.9 μV, we obtain a density of current 260E−3 A/cm^2, that corresponds to an electric field amplitude of 0.1 V/cm. The latter quantity is the electric field value that must be concentrated by the antenna and the whisker onto the rectifying junction.

We can now recall that the field enhancement capability of the 3D antenna coupled to the device, FE, was shown to be at least a value of 40,000 [11]. Simulations reported in [11] were performed in conditions of the ideal load, i.e. the whisker with radius of 50 nm distant 10 nm from a ground plane; such structure has an equivalent impedance different from that shown by the actual semiconductor device. The impedance of the designed rectifier can be evaluated from simulation reported in Fig. 3, as the ratio of applied voltage and current obtained with contact area equal to the whisker base area in the test structure, 100 nm × 100 nm. The high impedance of the device reduces the FE to a rather low value of 52. The combination of this result with the value of the electric field that must be induced into the junction to produce equivalent current allows the calculation of the external electric field reaching the antenna, and thus of the final value of the $NEP_{500\,\mathrm{GHz}} = 2.7\,\mathrm{pW}/\sqrt{\mathrm{Hz}}$, referred to the sample 4E. With the same procedure, we obtained $NEP_{500\,\mathrm{GHz}} = 1.7\,\mathrm{pW}/\sqrt{\mathrm{Hz}}$ for the sample 1C.

Taking into account the decrease of the rectified current with frequency shown by TCAD simulations, we obtain $NEP_{1\,\mathrm{THz}} = 10.8\,\mathrm{pW}/\sqrt{\mathrm{Hz}}$ for sample 4E, and $NEP_{1\,\mathrm{THz}} = 6.7\,\mathrm{pW}/\sqrt{\mathrm{Hz}}$ for sample 1C.

4 Conclusions

In this work, a new THz detector for direct conversion operating at room temperature and compatible with existing CMOS ISs is presented and experimentally evaluated. We demonstrate that a modification of a limited region of the surface of the CMOS ISs pixel, placed in contact with the metallic antenna pad, provides an efficient rectifying device in THz range. The antenna and the rectifying device, i.e. the rectenna structure, exposed to electromagnetic radiation gives rise to charge injection into the storage well of APS device that is evaluated by the readout electronics. We present measurements at a frequency of 40 GHz demonstrating the effectiveness of the rectifying device and confirming the rectification effect due to the formation of a double barrier just below the antenna whisker. Experimental results supported by 2D numerical TCAD simulations permit an evaluation of NEP at 1 THz. The experimental investigation at 1 THz of the device with the integrated antenna is the target of the future work.

Acknowledgements. The authors want to thank Aptina-OnSemi for allowing the realization of the test structure in the state-of-art CMOS ISs technology.

References

1. B. Fischer, M. Hoffmann, H. Helm, G. Modjesch, P. Jepsen, Chemical recognition in terahertz time-domain spectroscopy and imaging. Semicond. Sci. Technol. **20**, S246 (2005)
2. R. Piesiewicz et al., Short-range ultra-broadband Terahertz communications. IEEE Antennas Propag. Mag. **49**, 24 (2007)
3. F.J. Federici et al., THz imaging and sensing for security applications-explosives, weapons and drugs. Semicond. Sci. Technol. **20**, 266–280 (2005)
4. A. Menikh, S.P. Mickan, H. Liu, R. Maccoll, X.C. Zhang, Labelfree amplified bioaffinity detection using terahertz wave technology. Biosens. Bioelectron. **20**, 658–662 (2004)
5. K.M. Strohm, J. Buechler, E. Kasper, SIMMWIC rectennas on high-resistivity silicon and CMOS compatibility. IEEE Trans. Microwave Theory Tech. **46**, 669–676 (1998)
6. V. Varlamava, F. Palma, P. Nenzi, M. Balucani, Terahertz sensor for integrated image detector. Procedia Eng. **87**, 1131–1134 (2014)
7. P. Nenzi, F. Tripaldi, V. Varlamava, F. Palma, M. Balucani, On-chip THz 3D antennas, in *Proceedings of Electronic Components Conference* (2012), pp. 102–108
8. A. Del Monte, F. Palma, Italian Patent No. RM2014A000323 (2004)
9. E.R. Fossum, D.B. Hondongwa, A review of the pinned photodiode for CCD and CMOS image sensors. IEEE J. Electron Devices Soc. **2**, 33–43 (2014)
10. F. Palma, Italian Patent No. RM2010A000268 (2010)
11. V. Varlamava, F. Palma, P. Nenzi, M. Balucani, Electric field enhancement in 3-D tapered helix antenna for terahertz applications. IEEE Trans. Terahertz Sci. Technol. **4**, 360–367 (2014)
12. M.A. Stettler, M.S. Lundstrom, A microscopic study of transport in thin base silicon bipolar transistors. IEEE Trans. Electron Devices **41**, 1027–1033 (1994)